Astronomy & Astrophysics manuscript no. output
July 15, 2026

A numerical study of the interplanetary propagation of solar energetic particles with a three-dimensional heliospheric current sheet

Yuji Zhu[1,2], Xi Luo[1,⋆], Fang Shen[3,4], and Gang Li[5]

[1] Shandong Institute of Advanced Technology (SDIAT), 250100 Jinan, China
[2] Shandong University, 250100 Jinan, China
[3] State Key Laboratory of Solar Activity and Space Weather, National Space Science Center, Chinese Academy of Sciences, Beijing, China
[4] College of Earth and Planetary Sciences, University of Chinese Academy of Sciences, Beijing, China
[5] Institute of Space Science, Macau University of Science and Technology, Macau, China

ABSTRACT

Aims. We investigate how solar energetic particles (SEPs) propagate in the interplanetary space that includes the heliospheric current sheet (HCS). We also develop a new model for simulating SEP propagation more realistically and efficiently.

Methods. A magnetohydrodynamic (MHD) model was used to simulate the interplanetary background field that includes the HCS and solar wind structures. Additionally, the current sheet was reshaped in the model to reduce the impact of spurious magnetic reconnection in calculation results caused by numerical dissipation. The focused transport equation with a drift-motion term was employed to simulate the transport of SEPs in the interplanetary medium.

Results. The model can reproduce the characteristics of the curvature gradient drift of SEPs and the effects of HCS drift that are simulated with the test particle models. The effect of the HCS on the SEPs is significant. It includes an expanded transport range of SEPs in the longitudinal and latitudinal directions and exerts effects on the SEP flux profiles and energy. This numerical model was also used to reproduce a specific event. The HCS and solar wind structures affect the flux rise rate and peak value. The structured solar wind modulates key factors such as the drift velocity, energy evolution, and magnetic connection points, thereby altering the resulting particle flux. As the particle energy decreases, the HCS effect becomes increasingly weaker, whereas the effect of solar wind structures grows stronger.

Conclusions. Our model can simulate the SEP propagation near the HCS, based on the guiding center approximation theory. The greatest advantage of our model is that it incorporates the HCS and other interplanetary solar wind structures. For simulations of SEP events, it is crucial to take the roles of the HCS and solar wind structures into account.

Key words. Solar energetic particles(SEP) – Corotating interaction regions(CIR) – Magnetohydrodynamic(MHD)

1. Introduction

As humanity's space age expands, it is vital to study solar energetic particle (SEP) events because these events threaten satellites, communications, and astronauts in a growing number of deep-space missions(Feynman & Gabriel 2000). It remains a major challenge to predict SEP events, however, owing to the complex interplay of their seed populations, acceleration, and interplanetary propagation (Reames 2017).

During the propagation, SEPs are modulated not only by microscopic plasma turbulence, but also by large-scale long-lived interplanetary structures (Yermolaev et al. 2010). The heliospheric current sheet (HCS) is the structure among these stable macro-scale structures that separates regions of opposite magnetic polarity. It forms a warped spiral structure shaped by the Sun's dipole tilt, rotation, and solar wind propagation (Ness & Wilcox 1965; Smith 2001). Its structure has been extensively observed and studied (Thomas & Smith 1981; Hoeksema et al. 1983; Eselevich & Filippov 1988; Hoeksema 1995). Observations demonstrated the large-scale stability of the HCS at 1 AU throughout the solar cycle, and its thickness ranges between $\sim$ 600 km and 1.1×10^6 km (Liou & Wu 2021). Additionally, observations of the observed HCS crossings and predictions from potential field source surface (PFSS) and magnetohydrodynamic (MHD) models agree qualitatively (Szabo et al. 2020) .

The effect of the HCS on the SEP propagation has been a topic of discussion for decades. The analysis and statistical studies of observational data indicated that the fluxes, the onset, and the elemental abundance of SEPs are significantly affected after the HCS is crossed. The SEPs drop sharply when the coronal neutral line (i.e., HCS) is crossed in numerous low-energy (lower than 10 MeV) solar particle events (SPEs) (Roelof & Krimigis 1973; Liou & Wu 2024). The onset times (for about 0.5 MeV electrons) can be ordered by the occurrence of sector boundaries(Kallenrode 1993). The mean and median iron-oxygen ratio (Fe/O) values (for particles with about 0.5 MeV/nucleon) were found to be higher in the same-polarity group than in the opposite-polarity group, which crosses an HCS (Park et al. 2024). Recently, SEP acceleration near the innermost HCS region (< 0.1 AU) has been supported by evidence from Parker Solar Probe (PSP) observations (Desai et al. 2022, 2025; Phan et al. 2025).

⋆ Corresponding author: xi.luo@iat.cn

Article published by EDP Sciences, to be cited as https://doi.org/10.1051/0004-6361/202558591

The HCS can also indirectly affect SEPs. From a microscopic perspective, the HCS affects turbulence in the solar wind (Li et al. 2011; Shi et al. 2022; Wang et al. 2025), thereby affecting SEP propagation (Tsurutani et al. 1999; Zhang et al. 2025). From a macroscale perspective, the HCS can affect large-scale interplanetary structures such as coronal mass ejections (CMEs) or shocks, thereby affecting SEP events. Numerical simulation studies have shown that the HCS can affect interplanetary shocks (Steinolfson & Mullan 1980; Uralova & Uralov 1994; Wu et al. 2016). For example, the interaction of a CME-driven shock with the HCS can reduce the shock strength (Mach number), thus reducing the generation of SEPs (Wu et al. 2016).

Numerical simulation studies have also demonstrated the importance of the HCS in SEP propagation models. Test-particle simulations (Battarbee et al. 2017, 2018) proved that the HCS plays a governing role in SEPs (1–100 MeV), including longitudinal and latitudinal transport, time-profile complexity, and spectral hardening, with a dependence on the HCS tilt angle and the relative position between the source and the HCS. Follow-up simulations found that 3D effects associated with the HCS play a fundamental role in shaping the relativistic solar proton propagation to Earth (Dalla et al. 2020). Models that incorporate the HCS effect can reproduce the observed intensities near Earth for GLE events more accurately because most GLE events are associated with the HCS (Waterfall et al. 2022, 2025).

While numerous studies have demonstrated the importance of the HCS in the interplanetary transport of SEPs, significant gaps still remain in our understanding and prediction of the role of HCS in the propagation of SEPs. Most previous numerical simulation methods for SEP transport under the effect of the HCS have employed the test-particle method in the Parker spiral magnetic field (Battarbee et al. 2017; Dalla et al. 2020; Waterfall et al. 2025). However, the test-particle method is relatively computationally time-consuming because it needs to solve the Lorentz force equation for each particle. In studies of the Galactic cosmic-ray (GCR) propagation modulated by the HCS, the common approach is to incorporate a drift-velocity term in the Parker transport equation (PTE) (Burger & Potgieter 1989; Burger 2012; Strauss et al. 2012). This analytical approach reduces the computational cost and is more conducive to analysis. Furthermore, the use of the Parker field overlooks the effects of many other interplanetary structures, such as corotating interaction regions (CIRs). CIRs are formed when the fast solar wind catches the slow solar wind (Smith & Wolfe 1979), and the role of CIRs in modulating SEPs has been recognized (e.g., Richardson (2004); Cohen et al. (2020); Lario et al. (2022); Wei et al. (2022); Starkey et al. (2024)). CIR structures not only affect transport of SEPs, they can also accelerate suprathermal particles to become seed particles for further acceleration at CME-driven shock (Wijsen et al. 2023b). Notably, a statistical analysis of 216 HCS events revealed that 70.8% were followed by a stream-interaction region (SIR) within 36 hours (Xu & Xu 2024), underscoring the frequent co-occurrence of HCS and SIR structures. Furthermore, solar wind structures such as CIRs can interact with the HCS (Potapov 2018), and energetic particle intensity enhancement events have been observed in CIR structures embedded in the HCS (Silwal et al. 2024), further confirming that particle dynamics might be affected by the coupled large-scale solar wind and HCS structures. Therefore, simulations of the HCS modulating SEP propagation remain inadequate, and this severely limits the accuracy of space weather forecasting models.

To further explore the transport process of SEPs in complex interplanetary environments containing HCSs and solar wind structures and to construct SEP propagation models with more realistic backgrounds, we established a 3D MHD model coupled with focused transport equations (FTEs). By combining specific observational cases for analysis and comparison, this research aims to achieve a more comprehensive and in-depth understanding of SEP events, laying the foundation for a more accurate forecasting of space weather phenomena triggered by SEPs.

The structure of this paper is as follows: Section 2 briefly discusses the methods used in the model, including the background model and the SEP propagation model. Section 3 presents the results and discussion, where Section 3.1 investigates the effect of HCS modification on SEP model results, Section 3.2 focuses on the model performance in simulating the spatial distribution of SEPs in the background field that includes the HCS, Section 3.3 examines the model performance in simulating the effects of the HCS on the temporal profiles, pitch angles, and energy variations of SEPs at the observation site, and Section 3.4 describes the model performance in simulating real events. Finally, section 4 summarizes this paper and provides an outlook for future research.

2. Methods

2.1. Interplanetary model incorporating a 3D HCS

The interplanetary background was simulated using a magnetohydrodynamic (MHD) model. We simulated the background field following the method described in Shen et al. (2018). We obtained the background solar wind structure via the solution of the ideal MHD equations (Feng et al. 2003; Shen et al. 2009, 2007). The MHD equations are presented below,

$$\frac{\partial \rho}{\partial t} + \nabla \cdot (\rho \mathbf{V}) = 0, \tag{1}$$

$$\frac{\partial \rho \mathbf{V}}{\partial t} + \nabla \cdot [(\mathbf{P} + \frac{B^2}{2\mu_0})\mathbf{I} + \rho \mathbf{V}\mathbf{V} - \frac{\mathbf{B}\mathbf{B}}{\mu_0}] = -\frac{\rho G M_s}{r^3}\mathbf{r} + \mathbf{f}, \tag{2}$$

$$\frac{\partial \mathbf{B}}{\partial t} + \nabla \cdot (\mathbf{V}\mathbf{B} - \mathbf{B}\mathbf{V}) = 0, \tag{3}$$

$$\frac{\partial \mathbf{P}}{\partial t} + \nabla \cdot (\mathbf{P}\mathbf{V}) = -(\gamma - 1)\mathbf{P}\nabla \cdot \mathbf{V}, \tag{4}$$

where ρ denotes the mass density, $\mathbf{V}$ represents the solar wind velocity, $\mathbf{B}$ is the magnetic field vector, $\mathbf{P}$ stands for the thermal pressure, and γ is the ratio of specific heats. Since calculations are carried out in a reference frame corotating with the Sun, an additional fictitious force density vector, $\mathbf{f} = -\rho\Omega \times [\Omega \times \mathbf{r} + 2\mathbf{V}]$, is introduced, where Ω refers to the sidereal angular velocity of the Sun's rotation. As the solution domain varied from 0.1 AU to 10.0 AU, the radial grid resolution changed accordingly from 0.35 R_s to 6.19 R_s (with R_s denoting the solar radius). The angular resolution of the mesh was set to $1° \times 1°$.

To characterize the coronal magnetic field, we adopted the potential field source surface (PFSS) model (Schatten et al. 1969; Altschuler & Newkirk 1969). This model predicts the polarity of the interplanetary magnetic field very well, and subsequent magnetic field models have been further improved based on this framework. To set the radial velocity at the inner boundary, we employed a simplified WSA coronal solar wind model

(Arge et al. 2003). The inner boundary of the MHD model was positioned at 0.1 AU, with its boundary conditions specified by empirical formulas based on the PFSS model, WSA model, and the magnetic field observed at 1 AU (Shen et al. 2018). The boundary conditions at the inner surface remained fixed in the computation because the MHD background simulations were carried out in a reference frame that corotated with the Sun.

The magnetic fields were reshaped to minimize the occurrence of unphysical magnetic reconnection caused by numerical dissipation. To address this issue, we modified the inner boundary conditions and performed two independent simulation runs. The two runs shared identical numerical setups that only differed in the magnetic field polarities applied at the inner boundary. In the first run, radial unipolar magnetic field boundary conditions were applied to derive the large-scale configuration of the magnetic field lines. In the second run, we used the observed photospheric magnetogram as input to compute the realistic background magnetic field, and we further determined the orientation of the magnetic field lines and the location of the HCS, which was identified via magnetic polarity reversal. All other numerical parameters were kept strictly identical between the two runs. The final magnetic field configuration combined the field-line geometry from the first run with the magnetic field direction (polarity) from the second run. As shown in Fig. 1, the left panel is a schematic diagram of the magnetic field lines of the background field for Carrington rotation 1968 calculated by the original MHD model. This was a period of solar maximum. Due to numerical dissipation, multiple unphysical reconnections occurred in the magnetic field, which affected the SEP model results. The right panel presents the results of the modified background field, with fewer unphysical reconnections. The effect of the current sheet modification on the SEPs is discussed in more detail in Section 3.1.

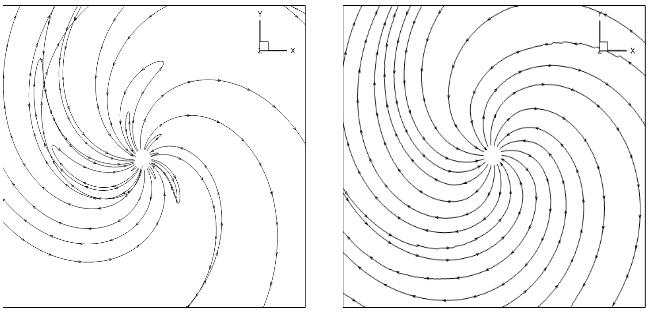

Fig. 1: Schematic diagrams of the magnetic field lines for CR1968 calculated with the original MHD model (left) and the modified result (right).

The heliospheric background simulated by this model automatically includes large-scale heliospheric structures (e.g., CIRs and the HCS). Figure 2 shows the shape of the HCSs and the solar wind speed calculated by the model. The left column corresponds to CR2206 (solar minimum), and the right column shows CR1968 (solar maximum). During CR2206, the tilt angle of the current sheet was lower than 20 degrees, maintaining a ballet-skirt-like shape as it extended into interplanetary space. During CR1968, the maximum tilt angle of the current sheet exceeded 50 degrees, and the morphology of the current sheet resembled a turbine. Our model can simulate the HCSs and the variations in solar wind during solar maximum and solar minimum. Therefore, this model has distinct advantages in simulating the propagation of SEPs in a more physically realistic heliospheric background field, one that is affected by a variety of large-scale structures.

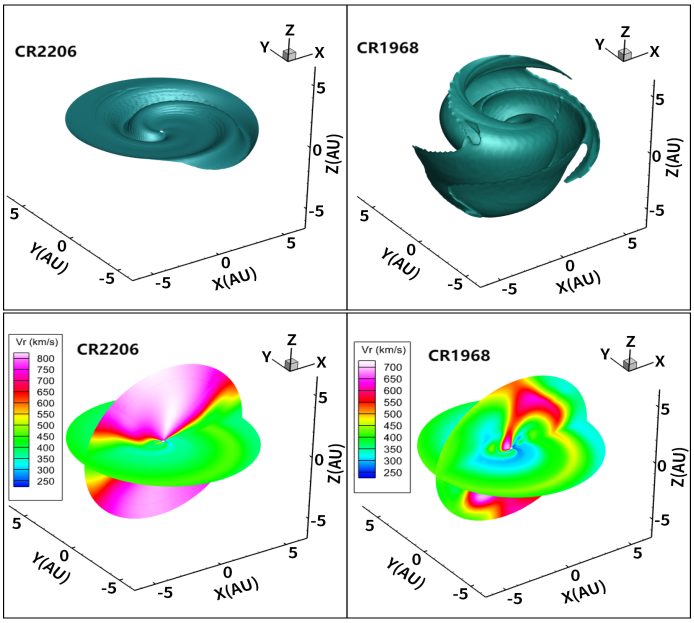

Fig. 2: Shape of the HCS (upper) and radial solar wind speed (lower) calculated with the model in a reference frame that corotates with the Sun. The left column corresponds to CR2206 (solar minimum), and the right column shows CR1968 (solar maximum).

2.2. SEP model

The focused transport equations (FTEs) were used to describe the particle transport, incorporating drift terms. The FTE for the particle distribution function can be written as (without the stochastic diffusion D_{pp}) (Skilling 1971; Isenberg 1997; Le Roux & Webb 2009; Zhang et al. 2009)

$$\frac{\partial f}{\partial t} = \frac{\partial}{\partial \mu} D_{\mu\mu} \frac{\partial f}{\partial \mu} + \nabla \cdot \kappa_{\perp} \cdot \nabla f - \frac{d\mathbf{X}}{dt} \cdot \nabla f - \frac{d\mu}{dt}\frac{\partial f}{\partial \mu} - \frac{dp}{dt}\frac{\partial f}{\partial p} + S, \quad (5)$$

where

$$\frac{d\mathbf{X}}{dt} = \mathbf{V} + v\mu\mathbf{b} + \mathbf{v}_d, \quad (6)$$

$$\frac{dp}{dt} = -[\frac{1-\mu^2}{2}(\nabla\cdot\mathbf{V} - \mathbf{bb} : \nabla\mathbf{V}) + \mu^2\mathbf{bb} : \nabla\mathbf{V}]p - \frac{\mu p}{v}\frac{d\mathbf{V}}{dt}\cdot\mathbf{b}, \quad (7)$$

$$\frac{d\mu}{dt} = \frac{(1-\mu^2)v}{2L_B} + \frac{\mu(1-\mu^2)}{2}(\nabla\cdot\mathbf{V} - 3\mathbf{bb} : \nabla\mathbf{V}) - \frac{1-\mu^2}{v}\frac{d\mathbf{V}}{dt}\cdot\mathbf{b}, \quad (8)$$

where $L_B^{-1} = -\mathbf{b} \cdot \nabla lnB$. $\mathbf{X}$, p, and μ are the particle spatial location, momentum, and cosine of the pitch angle, respectively. v is the particle speed. $D_{\mu\mu}$ is the pitch-angle diffusion coefficient. $\kappa_{\perp}$ denotes the cross-field diffusion coefficient. $\mathbf{b}$ is the unit vector of the magnetic field. $\mathbf{V}$ is the solar wind velocity. $\mathbf{v}_d$ is the particle drift velocity.

The form of $D_{\mu\mu}$ was chosen as (Qin et al. 2005; Zhang et al. 2009)

$$D_{\mu\mu} = D_0 v p^{-2/3}(1-\mu^2)\{|\mu|^{q-1} + h\}k(x), \quad (9)$$

where $k(x) = cos^2\psi = (B_r/B)^2$. We set h = 0.05, q = 5/3. The parallel mean free path is related to $D_{\mu\mu}$ through (Qin et al. 2005)

$$\lambda_{\parallel} = \frac{3v}{8}\int_{-1}^{+1}\frac{(1-\mu^2)^2}{D_{\mu\mu}}d\mu. \tag{10}$$

We set a constant radial mean free path $\lambda_r^{\parallel} = 0.3$ AU. We injected the protons at 0.1 AU (∼ 21 solar radii). The particles were assumed to be spatially uniformly distributed within the source region. The cross-field diffusion coefficient is expressed as

$$\kappa_{\perp} = \alpha v\lambda_{\parallel}\frac{\mathbf{B_0}}{\mathbf{B}}(\mathbb{I} - \mathbf{bb}), \tag{11}$$

where α is the free parameter, $\mathbb{I}$ is the unit tensor, and **b** is the unit magnetic field vector.

According to the classical guiding center motion theory (Burger et al. 1985), the velocity of the guiding center can be expressed as

$$\begin{aligned}\mathbf{v}_g =&\frac{\mathrm{d}\mathbf{x}_g}{\mathrm{d}t} = \mathbf{v} + \frac{\dot{\mathbf{p}}\times\mathbf{B}}{qB^2} + \frac{\mathbf{p}}{q}\times\frac{\mathrm{d}}{\mathrm{d}t}(\frac{\mathbf{B}}{B^2})\\ =&\mathbf{v} + \frac{\mathbf{E}\times\mathbf{B}}{B^2} - \mathbf{v}_{\perp} + \frac{\mathbf{p}}{q}\times\frac{\mathrm{d}}{\mathrm{d}t}(\frac{\mathbf{B}}{B^2})\\ =&\mathbf{v}_{\parallel} + \frac{\mathbf{E}\times\mathbf{B}}{B^2} + \frac{\mathbf{p}}{q}\times(\mathbf{v}\cdot\nabla)\frac{\mathbf{B}}{B^2}.\end{aligned}$$

After performing gyro-averaging on the particle motion, it can be expressed as

$$\begin{aligned}< v_g >_{\tau} =& < v_{\parallel} >_{\tau} + \frac{pv}{qB}\frac{1}{2}sin^2\theta(\nabla\times\frac{\mathbf{B}}{B})_{\parallel} + \frac{\mathbf{E}\times\mathbf{B}}{B^2}\\ &+\frac{pv}{qB}[\frac{1}{2}sin^2\theta\frac{\mathbf{B}\times\nabla B}{B^2} + cos^2\theta(\nabla\times\frac{\mathbf{B}}{B})_{\perp}],\end{aligned}$$

where $< v_{\parallel} >_{\tau}$ denotes the average velocity parallel to the magnetic field **B**, measured at the particle position. θ is the pitch angle of the particles. The other terms in the right-hand side of equation correspond to the particle drift velocity $\mathbf{v}_d$ and can be expressed as

$$\mathbf{v}_d = \frac{pv}{qB}cos^2\theta(\nabla\times\frac{\mathbf{B}}{B})_{\perp} + \frac{1}{2}sin^2\theta\frac{pv}{qB}[\frac{\mathbf{B}\times\nabla B}{B^2} + (\nabla\times\frac{\mathbf{B}}{B})_{\parallel}] + \frac{\mathbf{E}\times\mathbf{B}}{B^2}. \tag{12}$$

When the particles are isotropic, equation 12 can be simplified to the commonly used form in the GCR transport equation (Burger & Potgieter 1989; Burger 2012; Strauss et al. 2012; Potgieter 2013; Qin & Shen 2017),

$$< \mathbf{v}_d >_{\theta} = \frac{\mathbf{E}\times\mathbf{B}}{B^2} + \frac{pv}{3qB}[\frac{\mathbf{B}\times\nabla B}{B^2} + \nabla\times\frac{\mathbf{B}}{B}] = \frac{\mathbf{E}\times\mathbf{B}}{B^2} + \frac{pv}{3q}[\nabla\times\frac{\mathbf{B}}{B^2}]. \tag{13}$$

The interplanetary electric field was primarily treated as the solar wind motional electric field. Therefore, there is no electric field in the solar wind coordinate system, where particle velocities are calculated.

When particles reach the HCS, their gyration motion breaks down, and so does gyro-averaging. The current-sheet drift can be considered as an additional process. The formula following Burger (Burger et al. 1985; Burger & Potgieter 1989) was adopted,

$$V_{dc} = [0.457 - 0.412(\frac{x}{R_0}) + 0.0915(\frac{x}{R_0})^2]v, \tag{14}$$

where x is the distance between the particle and the HCS, R_0 is the Larmor radius, and v is the velocity of the particle. This formula was adopted when $x \leq 2R_0$. This formula is widely used in the calculation of the current sheet drift of GCRs (Strauss et al. 2012; Pei et al. 2012). It describes the drift of charged particles with an isotropic distribution near the current sheet. Given the strong turbulence intensity in the vicinity of the current sheet, we assumed that SEPs are isotropic there, and we thus adopted this formula. We then used Eq.12 to describe the drift velocity when $x > 2R_0$.

We then solved the FTE (Eq.5) with drift velocity V_d (Eq.12 or Eq.14) by the time-forward stochastic differential equation (SDE) (Bobik et al. 2016; Kopp et al. 2012; Strauss & Effenberger 2017). The corresponding forward SDEs are

$$\begin{cases} d\mathbf{X} = (\nabla\cdot\kappa_{\perp} + \frac{d\mathbf{X}}{dt})dt + \sqrt{2\kappa_{\perp}}dw_x,\\ dp = \frac{dp}{dt}dt,\\ d\mu = (\frac{\partial D_{\mu\mu}}{\partial\mu} + \frac{d\mu}{dt})dt + \sqrt{2D_{\mu\mu}}dw_{\mu}.\end{cases} \tag{15}$$

After the phase-space distribution function $f(x, y, z, p, \mu, t)$ was obtained, the particle differential intensity (per unit of kinetic energy) was calculated by

$$j_E = p^2 f_0(x, y, z, p, t), \tag{16}$$

where

$$f_0 = \frac{1}{2}\int_{-1}^{1} f(x, y, z, p, \mu, t)d\mu. \tag{17}$$

3. Results and discussion

3.1. The effect of the HCS modification

To demonstrate the role of the HCS modification in the MHD model (Section 2.1) that mitigates spurious unphysical magnetic reconnection from numerical dissipation, we injected SEPs into the background field before and after the reshaping. The magnetic polarity was positive (A=+1). The SEPs were 100 MeV protons that were injected impulsively at the inner boundary. The injection region spanned 10° in longitude and latitude. The center of the injection region was at the intersection of the HCS and the solar equator. Figure 3 presents the 100-hour-integrated fluence maps at 1 AU, where the dashed black lines in each panel indicate the position of the HCS at 1 AU at the time of particle injection.

As Fig. 3 shows, the model fails to reproduce the key characteristics of energetic particle drift when the HCS remains unmodified (the left columns), regardless of whether the HCS is flat (panel a)) or wavy (panel c)). When the HCS is flat under positive interplanetary magnetic field (IMF) polarity (A=+1), the particles are theoretically expected to drift toward the solar equator driven by the gradient-curvature drift. This fundamental behavior cannot be captured by the model before HCS modification (panel a)). For a wavy HCS in the A=+1 polarity configuration, SEPs should exhibit westward (rightward) motion along the current sheet. However, simulations without HCS modification erroneously predict eastward (leftward) particle transport instead (panel c)). In contrast, the model successfully reproduces the main dynamical features of SEPs when the HCS modification is applied (panels b) and d)).

To further elaborate, Fig. 4 plots the latitudinal variation in the longitudinal drift velocity component for 100 MeV protons in the flat HCS setup. The drift velocities were derived from Equation 12 and 14. The drift velocities for a pitch angle of 0° are nearly consistent between the two cases, whereas notable differences appear in the 90° pitch-angle drift velocities near the HCS after modification. The unphysical magnetic field line reconnection in the original model not only distorts the particle trajectories, but also skews the calculations of essential physical processes, such as the particle drift velocity. Therefore, it is essential to reshape the HCS on the original MHD background field to eliminate these numerical artifacts and to substantially improve the model capability to realistically simulate SEP transport near the HCS.

3.2. The fluence map

The spatial distribution of SEPs was investigated by injecting particles under various configurations of IMF. Protons with 100 MeV were impulsively injected at 0.1 AU. The injection region was centered at the solar equator and had a size of 10° × 10°. About $\sim 1{\times}10^5$ particles were traced in each case. The particle fluence, quantified as the number of particles per unit area and per unit solid angle over a duration of 100 hours, was recorded, and a spatial fluence map was subsequently generated.

Figure 5 presents 100-hour SEP fluence maps at 1 AU, designed to quantify the effects of different background magnetic fields and HCS configurations on SEP propagation. The left column (panels A1, B1, and C1) displays simulation results under the Parker field background (Parker 1958), and the right column (panels A2, B2, and C2) shows results under the structured solar wind background.

We first examined the no-HCS baseline scenario, which isolates the effect of the background solar wind field without HCS-related effects. Panel A1 shows results for a unipolar outward Parker field: the highest fluence (dark red region) lies in the area that is magnetically well connected to the particle source, and the overall fluence distribution shifts westward (rightward) due to solar corotation. By contrast, panel A2 shows the structured solar wind case: while the large-scale background magnetic field remains longitudinally uniform, the solar wind exhibits a latitudinal speed gradient, with slower wind speeds at lower latitudes. This gradient produces the bow-shaped well-connected region (dark red), as slower solar wind creates more tightly wound Parker spiral field lines (via the magnetic frozen-in effect) that intersect the 1 AU sphere at more easterly longitudes. On the other hand, the southward particle drift driven by the gradient-curvature drift is significantly more pronounced in this structured background than in the Parker field. This is primarily due to the different magnitudes of the magnetic fields in the two background fields (see Eq. (13) and (17) in Dalla et al. (2013)). Controlled by magnetic flux freezing, the magnetic field varies with solar wind speed. Consequently, the two background configurations yield distinct magnetic field magnitudes. The computed southward drift from the MHD solution is not universally stronger than that derived from the Parker field.

We next introduced a flat HCS aligned with the solar equator (panels B1 and B2, marked by the dotted black line) to resolve the additional effect of HCS-associated drift on SEP propagation. Here, the IMF has a positive polarity (A=+1): for this polarity, gradient-curvature drift drives SEPs toward the solar equator, while the HCS drift further induces westward (rightward) particle motion near the current sheet, enabling SEPs to propagate to a wider longitudinal range. Compared with the Parker field case (panel B1), SEPs in the structured solar wind (panel B2) exhibit a broader westward drift range along the HCS, with their spatial distribution more tightly concentrated toward the current sheet.

Finally, we considered the more realistic wavy HCS configuration (panels C1 and C2), which better matches in situ observed HCS structure. Owing to HCS drift, particles propagate along the curved current sheet and can thus reach higher latitudes. In the structured solar wind (panel C2), the SEP fluence distribution is more confined to the HCS, with the high-fluence region (red and yellow) closely following the curved path of the current sheet. In contrast, the Parker field case (panel C1) shows larger latitudinal deviations from the HCS. Furthermore, SEPs in the structured solar wind show a greater drift extent along the HCS, with the fluence distribution extending to larger longitudes than in the Parker field.

To quantitatively explain the above differences in SEP propagation and fluence distributions, Figure 6 shows the latitudinal variation of drift velocities for 100 MeV protons under the same set of configurations. The drift velocities were derived from Equation 12 and 14. The three rows from top to bottom correspond to the radial, longitudinal, and latitudinal components of the drift velocity, respectively. For the Parker field (blue lines), the drift velocities vary little between the two pitch angles (dashed vs. solid lines). For the structured solar wind (red lines), however, the drift velocities deviate significantly from the Parker field curves, most notably, for particles with a 90° pitch angle (solid red lines). In Eq. 12, for $\theta = 0°$, the discrepancy in v_d between the two field configurations primarily arises from the term $\frac{1}{B}\nabla \times \frac{\mathbf{B}}{B}$. The unit magnetic vector $\mathbf{b}$ evolves similarly in both fields. For $\theta = 90°$, the term $\frac{\mathbf{B}\times\nabla B}{B^2}$ plays a role. Owing to the magnetic flux freezing effect, solar wind speed variations alter the magnetic field. This produces distinct ∇B values in different background field models. Consequently, the drift velocity under the structured solar wind deviates substantially from the Parker field at a 90° pitch angle.

This velocity difference directly explains the SEP distribution features in Figure 5. In the structured solar wind, the absolute values of the latitudinal drift velocity (panels B1, B2, and B3 in Fig. 6) are considerably higher, which accounts for the prominent southward particle drift in panel A2 of Figure 5, and the tighter confinement of SEPs to the HCS in panels B2 and C2 of the same figure. In the presence of an HCS, particles exhibit intense westward longitudinal drift ($vd_\phi > 0$) at the HCS position (horizontal coordinate = 0), as shown in panels C2 and C3 in Fig. 6. At a pitch angle of 90°, the longitudinal gradient-curvature drift velocity shown in panel C2 is negative in the Parker field (solid blue line). In contrast, this drift becomes positive in the structured solar wind case (solid red line in panel C2), excluding latitudes within ±1° from the HCS. This positive drift matches the direction of the HCS drift. It accounts for the enhanced westward particle transport in panel B2 of Figure 5 compared to panel B1. The negative longitudinal gradient-curvature drift near the HCS might originate from the computational method. We adopted a 1° grid resolution and used central differencing to compute the gradient terms for the drift velocities.

Furthermore, the HCS polarity and the relative position between the SEP source and the current sheet also affect SEP transport (Battarbee et al. 2017, 2018; Waterfall et al. 2022). The re-

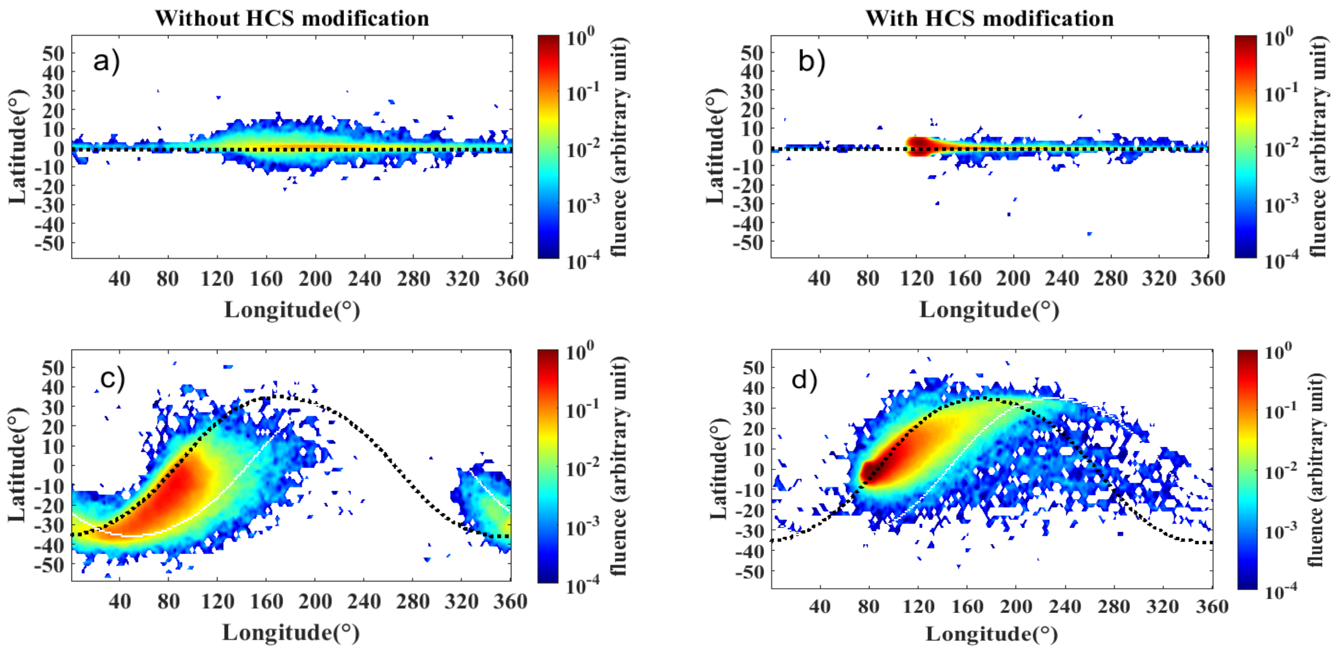

Fig. 3: SEP fluence maps (for 100 hours) at 1 AU for the background calculated for the HCS without modification (panels a) and c)) and the modified HCS (panels b) and d)). The magnetic polarities are A=+1. Panels a) and b) show the results with a flat HCS, while panels c) and d) show this with a wavy HCS. The color maps illustrate the intensity integrated over 100 hours at 1 AU for protons injected with 100 MeV, using a logarithmic scale. The dashed black lines in each panel denote the position of the HCS at 1 AU at the time of particle injection. The dashed white line in panels c) and d) is the position of the HCS after 100 hours.

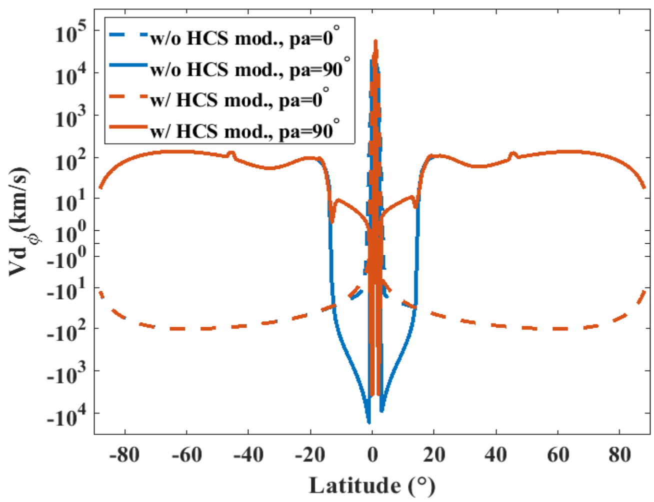

Fig. 4: Latitudinal variation in the longitudinal drift velocity component (derived from Equation 12 and 14) for a flat HCS under positive polarity (A = +1). The blue and red lines represent the results before and after HCS modification, respectively. The dashed and solid lines correspond to pitch angles of 0° and 90°, respectively.

sults for different magnetic polarities and injection locations are presented in Figure 7. Panel a) of Fig. 7 illustrates the particle fluence distribution obtained in the A=-1 magnetic field. The particles drift eastward and toward the polar regions under negative magnetic polarity. Panel b) in Fig. 7 shows the simulation results when particles are injected entirely north of the solar equator within the A=+1 magnetic field. The results demonstrate that the HCS acts as a barrier that prevents particles from crossing the current sheet. On the one hand, strong HCS drift motions near the HCS drives particles along the current sheet to other longitudes. On the other hand, gradient–curvature drift drives particles toward the solar equator. Combined, the number of particles crossing the current sheet was significantly reduced. These results agree with previous work in Battarbee et al. (2017).

In summary, the spatial distribution of SEPs is jointly controlled by multiple factors, including HCS geometry, magnetic polarity, and the relative location of the injection region with respect to the HCS. Our simulation reproduced the major key features reported in previous test-particle model studies (Battarbee et al. 2017, 2018). Moreover, large-scale solar wind structures also play a vital modulating role in the SEP propagation.

3.3. Time profile and energy variation

We then examined the HCS effect on in situ observations of SEPs. Particles were injected under the Parker field and structured solar wind backgrounds. The injection region measured $10^\circ \times 10^\circ$, and its injection center lay on the HCS at 0.1 AU. With the well-connected magnetic field line of the injection center at 1 AU positioned at longitude 0° and latitude 0°, the observers were located at longitude $30^\circ W$ and latitude 0° at 1 AU. It follows that the observer was not directly connected to the injection region. The temporal variation in flux and energy distribution at the observation site were recorded.

Figure 8 shows the variation in particle flux (40-100 MeV) with time. Panel a) shows the simulation results for the Parker field, and panel b) presents those under the structured solar wind. In the Parker field (panel a) of Fig. 8), the solid blue line represents the time profile without the HCS. Particles mainly reach the west of the injection region due to corotation and curvature-

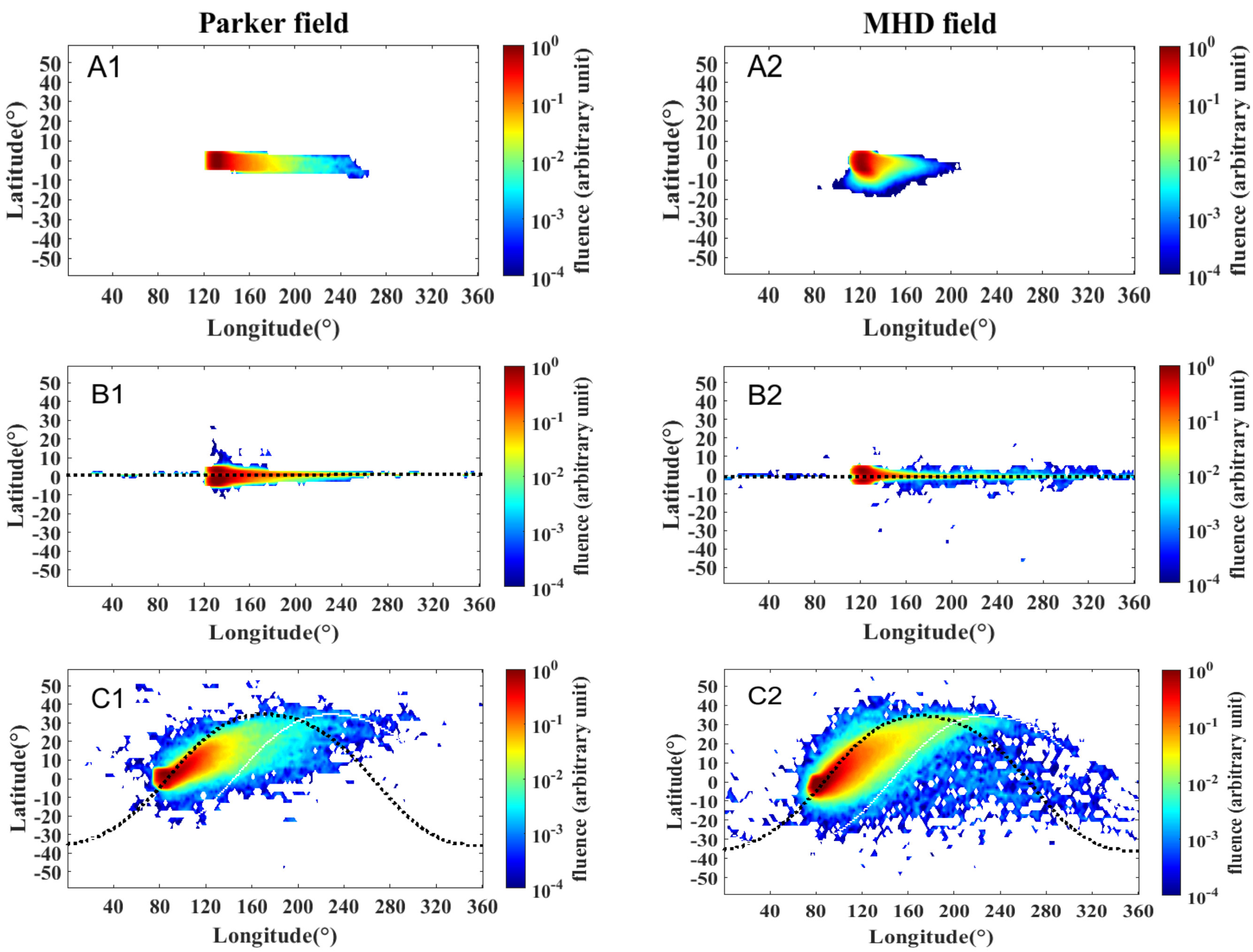

Fig. 5: SEP fluence maps (for 100 MeV protons injected) at 1 AU in different IMF conditions. Panels A1, B1, and C1 present the results under a Parker field, while panels A2, B2, and C2 present the results under a structured solar wind field. Panels A1 and A2 present the results for unipolar outward magnetic fields. Panels B1 and B2 show the results for a background with a flat HCS (A = +1). Panels C1 and C2 display the results for a background with a wavy HCS (A = +1). The color maps illustrate the flux intensity values integrated over 100 hours, using a logarithmic scale. The dotted black lines in each panel denote the position of the HCS at 1 AU at the time of particle injection. The white lines in panels C1 and C2 represent the HCS after 100 hours.

gradient drifts. The onset time of the event is approximately 14 hours after the injection. The red line shows the case with a flat current sheet (A=+1). Owing to the drift effect of the current sheet, particles can be detected within 4 hours after injection, and the peak value of the particle flux is also higher. The yellow line represents the flux under the effect of a wavy HCS. The observed peak intensity is lower than in the previous two cases, since more particles propagate along the wavy HCS to higher latitudes. Nevertheless, owing to the westward particle motion induced by the HCS drift, the event onset time remains earlier than in the case without the HCS.

Panel b) of Fig. 8 presents the results for the structured solar wind. The observation points are at 30° west of the well-connected magnetic field line at 1 AU in all cases. Therefore, variations in the magnetic well-connection point caused by different solar wind speed have negligible effects on the differences in flux profiles. For each HCS configuration, the peak intensity is generally similar to that obtained in the Parker field. However, the flux peak time and event duration differ from the Parker field results. Most notably, the wavy HCS case (yellow line) yields a longer event duration than the Parker field and presents a double-peak profile. The first flux detection occurs because curvature-gradient drifts impart a significant westward drift velocity to particles outside the HCS. The flux decreases then as no new particles are replenished, and curvature-gradient drifts drive particles toward the HCS. The second peak arises from the westward corotation of the HCS with the Sun. The HCS vicinity still stores numerous particles that drift along the sheet, even when particles outside the HCS are depleted. This phenomenon does not occur in the Parker field, likely because the drift velocities, as analyzed above, confine the particles more tightly near the HCS in the structured solar wind than in the Parker field.

In addition to drift process, the observed profiles might also be affected by energy variations during particle propagation. To investigate the effect of the HCS on particle energy, we analyzed the energy distribution of particles at 1 AU after an impulsive injection (with an initial energy of 100 MeV) at the inner boundary.

Figure 9 shows contour plots of particle intensity obtained on the spherical surface at 1 AU from the Sun for different IMF configurations. Each panel corresponds to the identically numbered panel in Figure 5. Due to the adiabatic cooling effect, particles

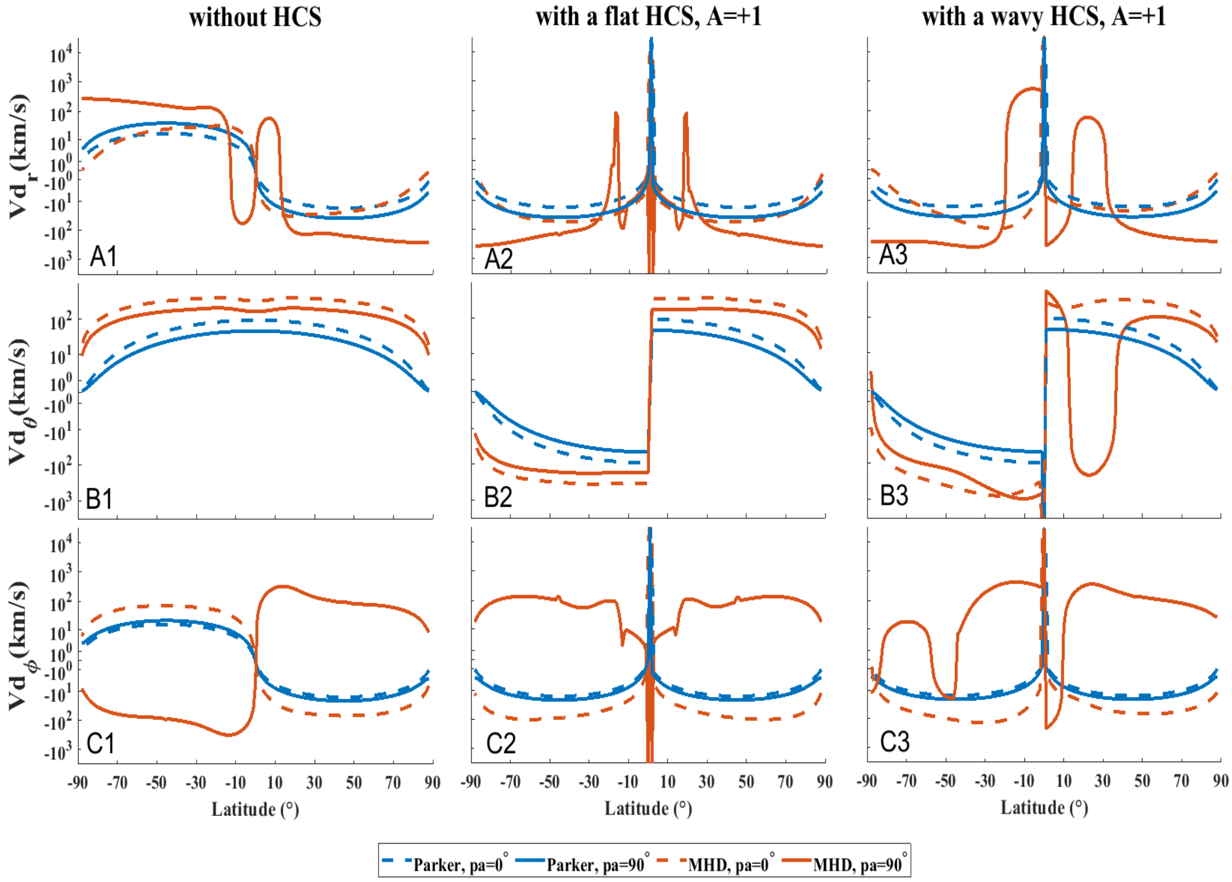

Fig. 6: Latitudinal variations in the drift velocity components for 100 MeV protons derived from Equation 12 and 14. The rows from top to bottom show the radial (Vd_r), latitudinal (Vd_θ), and longitudinal (Vd_ϕ) drift velocity components, respectively. The columns from left to right correspond to three scenarios: no HCS, a flat HCS, and a wavy HCS. For the wavy HCS case, this value is taken at a specific longitude at which the HCS lies exactly at latitude zero. The magnetic polarities are positive (A=+1). The blue lines represent the Parker field case, and the red lines denote the structured solar wind case. The dashed and solid lines indicate particle pitch angles of 0° and 90°, respectively.

experience an energy decrease during their interplanetary propagation. Under the unipolar outward magnetic field configuration (panels A1 and A2), the energy of 100 MeV protons at injection is reduced to approximately 60 MeV when they reach 1 AU after 100 hours. Variations in the solar wind speed produce different adiabatic cooling effects, leading to slight discrepancies between panels A1 and A2. In the case of a flat HCS, more low-energy particles can be observed at early times in the Parker field (panel B1) than in the HCS-free scenario. By contrast, the duration of the observed particle events is shortened in the structured solar wind (panel B2). In this case, particles are more tightly confined near the flat HCS and undergo stronger radial outward drift (see panel A2 in Fig. 6), which advances their arrival time. In the case of a wavy current sheet, the energy distribution of particles arriving at 1 AU at a given time becomes much broader under the structured solar wind (panel C2), whereas no such broadening occurs in the Parker field (panel C1). The reason might be that in the background field of the curved current sheet, particles can move to a wider range of latitudes. In the structured solar wind, particles can undergo distinct adiabatic cooling processes and propagate along paths of different lengths under varying solar wind speeds.

Our results indicate that the HCS modifies the particle energy evolution during the propagation. This effect becomes even more pronounced when combined with variations in solar wind speed.

3.4. Simulation of specific events

To validate our model, we simulated a ground-level enhancement (GLE) event. We selected the observed proton flux data from the GOES-11 satellite between January 20 and 23, 2005, for comparison (GLE 69). The injection location of the associated flare was positioned at N14W63 in this event. The footpoints of the flare and the observation site in this event were both near the current sheet, and thus, might have been significantly affected by the drift motion along the current sheet (Grechnev et al. 2008; Waterfall et al. 2022). Figure 10 shows the location of the flare and Earth's footpoint, superimposed on the distribution of solar wind speed (the color map) and the shape of the HCS (the dotted white line) at 0.1 AU in our model.

We injected the protons at 0.1 AU. The size of the injection region was 30°×30° (following the set of Waterfall et al. (2025)). The particles were uniformly injected. The injection time profile was assumed to be (Reid 1964)

$$f_b(t) = Q_0 \frac{1}{t} exp\{-\frac{\tau_c}{t} - \frac{t}{\tau_l}\}, \tag{18}$$

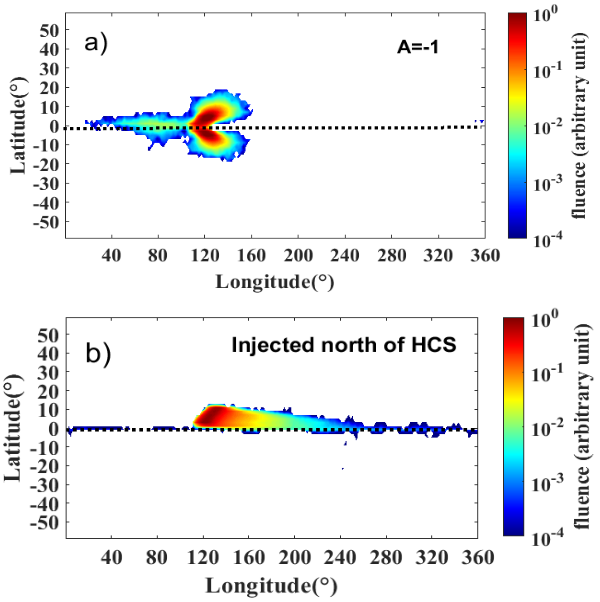

Fig. 7: Same as panel B1 in Fig. 5, where only the magnetic polarity is set to A=1 in panel a), and only the particle injection location is adjusted to be entirely north of the solar equator in panel b).

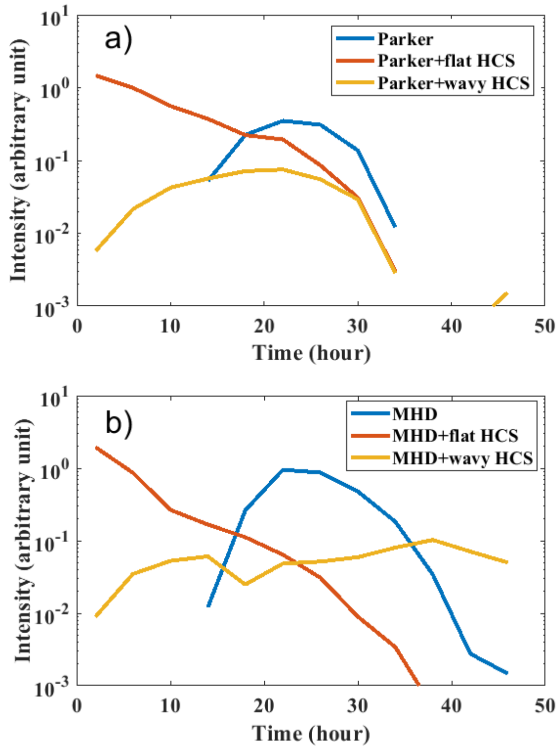

Fig. 8: Profiles of SEP flux (40-100 MeV) variation with time in situ observation at 1 AU. The source region is $10° \times 10°$. The observer is located 30° west of the well-connected point of the center of the source region at 1 AU. The blue lines represent the cases without a current sheet, the red lines represent the cases where the background field includes a flat current sheet, and the yellow lines represent the cases where the background field includes a curved current sheet. Panel a) shows the scenario in the Parker field, and panel b) shows the scenario in the structured solar wind.

where τ_c and τ_l are the rise and decay timescales of the injection time profile, respectively. Q_0 is a constant. τ_c was assumed to be 0.05 days, and τ_l was assumed to be 0.01 days (to simulate an impulsive injection). We examined protons in the energy ranges of 350–420 MeV, 40–80 MeV, and 4–9 MeV. For particles in these three energy ranges, we injected particles with energy ranges of 300–500 MeV, 30–100 MeV, and 1–15 MeV, respectively. The spectral index for the power-law fits was assumed to be −1.5. About ~ $7{\times}10^6$ particles were traced in each case.

Figure 11 shows the model simulation results of the 350-420 MeV proton flux time profiles observed by GOES during GLE 69. The magnetic polarity in this event was negative (A=-1), and the particles are expected to drift eastward (leftward) along the HCS. Notably, the peak particle flux increases by nearly two orders of magnitude considering the drift effects (the solid blue line), particularly, the significant HCS drift. The flux increase under drift effects is also steeper. To explore the role of solar wind structures, we also constructed a Parker spiral field as the background field. This Parker field had a uniform solar wind speed ($400 kms^{-1}$). We extracted the structure and position of the HCS from the original MHD field and embedded it into this Parker field. The dotted purple line in Fig.11 is the result in the Parker field with the HCS extracted from the MHD background. Even the HCS drift effect was included, and the peak particle flux in the Parker field was lower by about one order of magnitude than that in the structured solar wind background. The possible reasons are discussed in greater detail when we present the results for lower-energy particles below. Additionally, the particle flux rises at a lower rate, and its peak arrival time is delayed. Therefore, the HCS drift and solar wind structures play an important role when SEP events are simulated.

To more intuitively demonstrate the role of the HCS and solar wind structures, simulated fluence maps of 350-420 MeV protons at 1 AU are plotted (Fig. 12). Panels A and B depict the results under the MHD background. Panel A corresponds to the result with drift effect and Panel B to that excluding the drift effect (the drift velocity V_d was set to be zero). In panel B, particles propagate across the magnetic field only due to the cross-field diffusion implemented in the model. In panel A, due to the drift effect of the HCS, the protons drift eastward (leftward) along the HCS. This significantly alters the spatial distribution of protons, causing them to move to wider longitudes and higher latitudes. Panel C corresponds to the case of the Parker field embedded with the HCS. The results agree with those of Waterfall et al. (2022) (the upper panel in their Figure 9) obtained with a model that used the Parker field. The dark red regions are those with the best magnetic connection to the source region. Under the Parker field with uniform solar wind speed, the positions with the best magnetic connection at 1 AU resemble the shape of the source region ($30° \times 30°$ square). However, after considering the solar wind structures (panels A and B), the shape of this region at 1 AU changes through the magnetic frozen-in effect. In the slower solar wind, magnetic field lines are more tightly wound, so variations in solar wind speed deform the well-connected region.

We also attempted to simulate particle fluxes in lower-energy ranges. Figure 13 is similar to Fig. 11, but for 40-80 MeV (upper) and 4-9 MeV (lower) protons. When drift effects are not considered (dashed red lines), the peak intensity is lower for 40–80 MeV and 4–9 MeV particles. More specifically, compared with the scenario where drift effects are included, the peak intensities of particles of 350–420 MeV, 40-80 MeV, and 4-9 MeV are

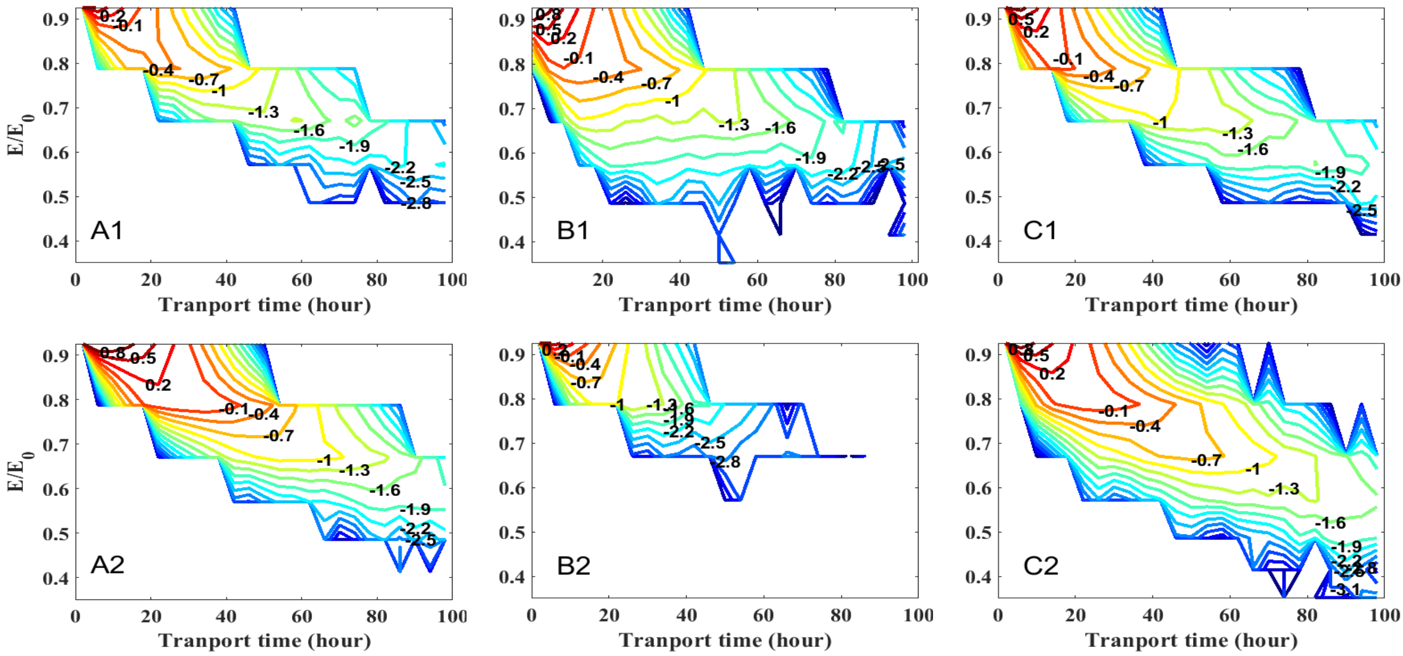

Fig. 9: Contour plots of intensity at 1 AU on a logarithmic scale as a function of the transport time and energy for different IMF configurations. The color indicates the particle intensity obtained on the spherical surface at 1 AU from the Sun. The logarithmic exponents of the intensity are labeled on the contours. X-axis: Particle propagation time from release to 1 AU. Y-axis: Ratio of the particle energy at 1 AU to injected energy (E_0=100 MeV). Each panel corresponds to the conditions of the identically numbered panel in Figure 5.

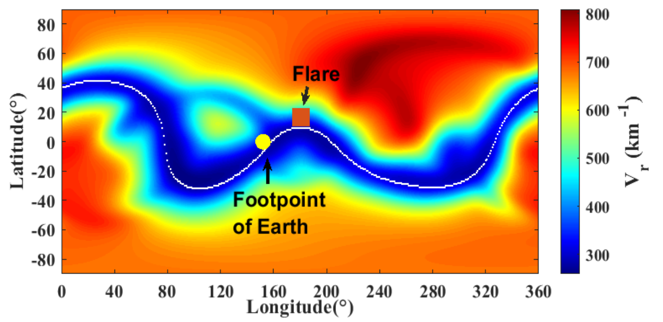

Fig. 10: Flare location (red square) and Earth's footpoint (yellow circle) superimposed on the solar wind speed distribution (color map) and HCS shape (dotted white line) at 0.1 AU in our model.

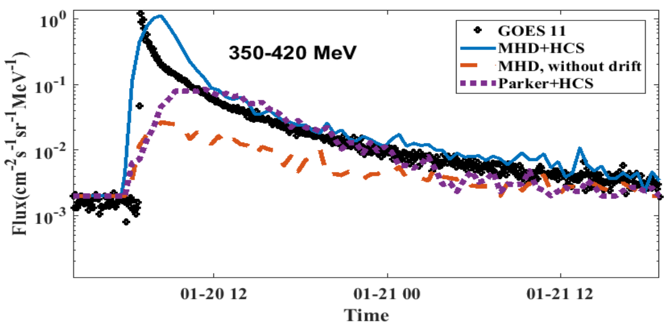

Fig. 11: Simulation of the 350-420 MeV proton flux time profiles observed by GOES during GLE 69. The black circles represent the results of GOES-11 observations taken every five minutes. The solid blue line represents the results in the MHD background embedded with the HCS. The dashed red line represents the results in the same solar wind structure, but without drift effects. The dotted purple line is the result in the Parker field with the HCS extracted from the MHD background.

reduced by 97.2%, 94.6%, and 83.3%, respectively. This indicates that as the energy decreases, the drift effects on the peak intensity gradually weaken. Nevertheless, our simulation results show that drift effects remain important even for particles with energies as low as several MeV.

When considering the HCS drift effect but excluding the role of solar wind structures (dotted purple lines), we cannot simulate the enhancement of 4–9 MeV and 40–80 MeV particle fluxes observed in this event. To clarify whether these effects arise from variations in magnetic connectivity, we plot the spatial distribution of the simulated peak flux of 40–80 MeV particles around the observation point, as presented in Figure 14. The left panel shows the results in the Parker field, and the right panel corresponds to the structured solar wind. In the figure, dark red areas denote locations with well magnetic connectivity to the source region. Solar wind structures significantly modify the position of well-connected regions. In the Parker field, the well-connected regions is located approximately 15° west of the observation point, whereas it shifts to roughly 7° west in the structured solar wind. Nevertheless, differences in observed flux profiles are affected not only by the magnetic connectivity. In the Parker field (left panel), the peak flux of 40–80 MeV particles drops to the background intensity at a longitudinal distance of about 15° away from the well-connected regions. By contrast, in the structured solar wind (right panel), peak fluxes exceeding the background intensity by one order of magnitude can still be observed at longitudes over 25° east of the well-connected region.

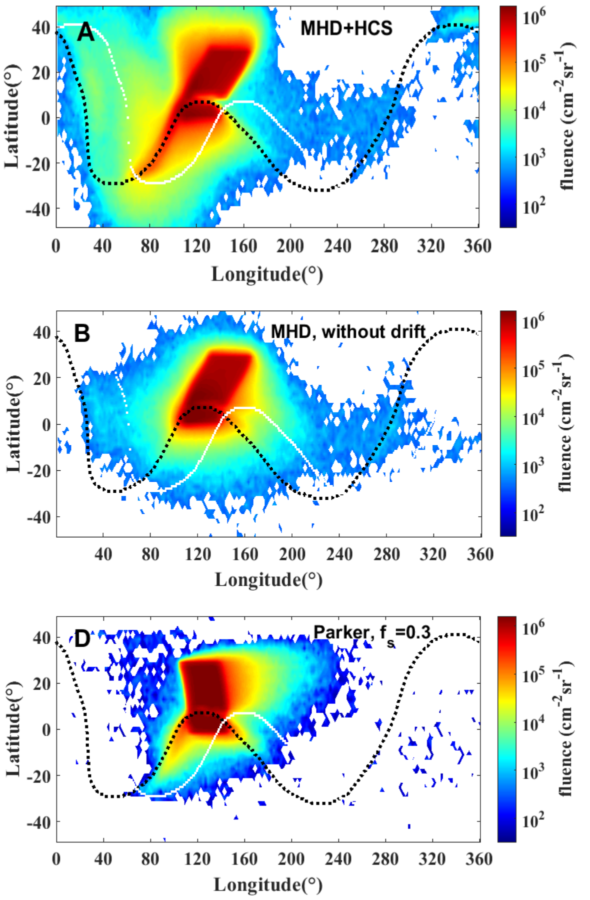

Fig. 12: Fluence map for 350–420 MeV SEPs at 1 AU over 60 hours in the GLE 69 simulations. Panels A and B show the results with the MHD background. Panel A corresponds to the results with the drift effect, and panel B shows those without the drift effect. Panel C shows the result in the Parker field embedded the HCS. The dashed black lines indicate the position of the HCS at the time of the flare injection, while the white lines indicate its position 60 hours later.

Thus, solar wind-speed-induced changes in magnetic connectivity are insufficient to explain the differences in flux profiles between the two background environments. Other factors, such as variations in particle drift velocity (Section 3.2) and energy variation (Section 3.3), also exert substantial effects. These results demonstrate that solar wind structures play a more critical role for particles with lower energies, especially those below several dozen MeV.

The work on the effect of the ambient solar wind medium on a CME-driven shock (Wijsen et al. 2023a) also indicates the effect of even modest background solar wind structures on the development of SEP events (for ions with energy $\leq$ 5 MeV). In summary, as the particle energy decreases, the HCS drift effect on the SEP intensity becomes increasingly weaker, while the role of solar wind structures becomes more prominent.

Our simulation results indicate that when the effects of HCS drift and solar wind structures are considered together, the observed curve can be better simulated. Our simulation does not reproduce the GOES observation data exactly because of multiple factors. First, the real particle source might differ from our setup. The event was accompanied by a CME (Grechnev et al. 2008), whereas we only assumed instantaneous injection at the inner boundary (0.1 AU). The results can also change when the particles are injected closer to the Sun. Second, the interplanetary micro-conditions might not match our settings. We assumed that the radial mean free path $\lambda_r^{\parallel}$ = 0.3 AU is a constant value, and the form of the cross-field diffusion coefficient (see equation 11, where in our model $\alpha = 10^{-4}$ is constant) is rather simplistic. Third, GOES satellite observations can be affected by the Earth's magnetic field. Its effect on lower-energy particles is particularly significant. This factor is not accounted for in our model. We need to improve and refine our model to make the predictions more accurate.

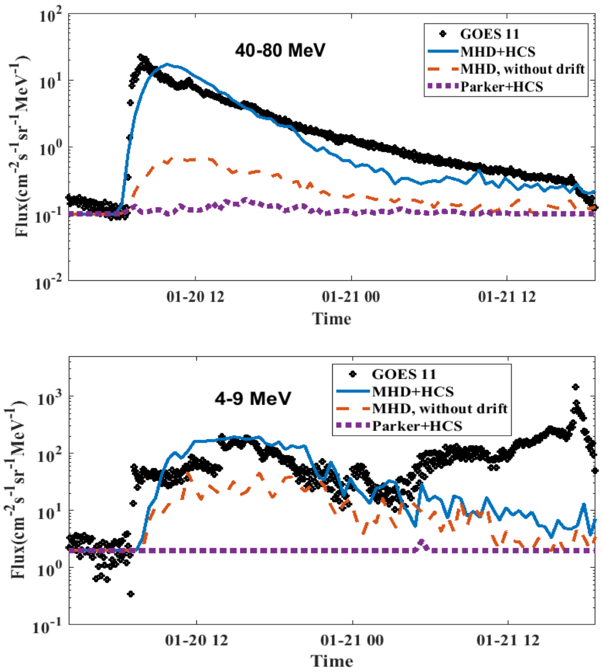

Fig. 13: Similar to Fig. 11, but for SEPs with 40–80 MeV (upper) and 4–9 MeV (lower).

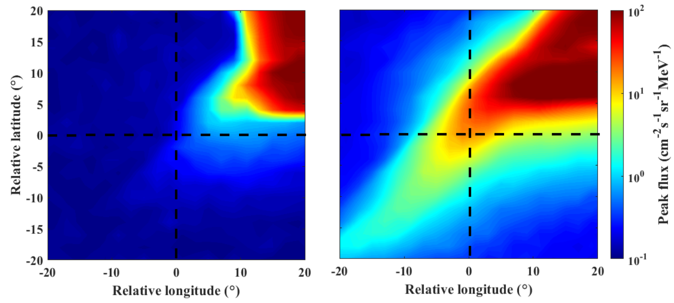

Fig. 14: Peak intensity distribution of 40–80 MeV protons around the observation point. The point [0, 0] in these figures corresponds to the observation location in Fig. 13. The left panel corresponds to the Parker field, and the right panel shows the structured solar wind condition.

4. Summary and conclusions

We established a 3D numerical model to investigate the interplanetary propagation of solar energetic particles (SEPs) in an environment containing the heliospheric current sheet (HCS) and other large-scale solar wind structures to improve the realism and efficiency of SEP propagation simulations. The model couples a magnetohydrodynamic (MHD) background field model with the focused transport equation (FTE) incorporating drift motion terms, and we validated its performance through systematic simulations and a case study of a ground-level enhancement (GLE) event (GLE 69).

The MHD model we used to simulate the interplanetary background field is based on the ideal MHD equations, with the inner boundary conditions specified using empirical formulas and a simplified WSA coronal solar wind model to characterize the radial velocity. Furthermore, to minimize unphysical magnetic reconnection caused by numerical dissipation in the original MHD results, we performed two independent simulation runs with identical numerical setups, but different inner boundary magnetic polarities. One run derived the large-scale magnetic field line geometry, and the other run determined the magnetic polarity and HCS location. The results were combined to obtain the final magnetic field configuration. Our results indicate that this correction is necessary. Otherwise, the numerical artifacts would distort the SEP drift trajectories and yield results that contradict the theories. Focused transport equations incorporating drift motion terms were used to describe the particle distribution function. The drift velocity was calculated based on the guiding center motion theory. Since the guiding center motion theory can break down at the HCS, a specific formula for the current sheet drift was adopted when particles were within 2 Larmor radii of the HCS.

Our model can describe the main characteristics simulated by previous $SEP + HCS$ models (e.g., Battarbee et al. (2017, 2018)). Particles drift to farther longitudinal positions along the current sheet and can drift to higher latitudinal positions under a curved current sheet. Under the $A+$ ($A-$) IMF polarity, particles drift toward the current sheet (the poles). The current sheet exerts a blocking effect on particles crossing it. Furthermore, our results indicate that solar wind structures also exert a significant effect on the propagation of SEPs near the HCS. Solar wind structures modulate the particle drift velocity, energy variation (especially in the presence of the HCS), and the magnetic connectivity to the source region, thereby affecting the observed variations in SEP flux. We also verified the model by simulating a specific event. In GLE 69, the HCS affected the spatial distribution of SEPs and improved the accuracy of our intensity prediction of the SEP event. Solar wind structures also play an important role in SEPs, especially for those with lower energy (below 100 MeV). Therefore, it is crucial to incorporate the HCS and solar wind structures in the considerations for SEP event prediction.

Compared with previous SEP transport models that incorporated the HCS (Battarbee et al. 2017, 2018; Dalla et al. 2020; Waterfall et al. 2022, 2025), our model adopted a distinct approach for particle transport and further accounted for the effects of solar wind structures. Previous models adopted the test-particle approach, directly using the Lorentz force formula to describe individual particles. Our model uses a distinct approach based on the probability distribution function to describe SEPs, and it further incorporates the effects of realistic solar wind structures instead of the ideal Parker field. Although our model may be less precise and detailed in describing individual particle behavior compared with test-particle models, it accounts for a more complete set of large-scale background structures, making it more consistent with the realistic interplanetary conditions under which SEP propagation takes place.

Compared with previous MHD–based SEP studies (Wijsen et al. 2020, 2023a; Houeibib et al. 2025), our model explicitly incorporates the role of the HCS structure, which has seldom been addressed in previously MHD–based investigations. However, our model currently only considers protons and neglects the role of the dynamic evolution of the background field. Electron contributions (Houeibib et al. 2025), as well as dynamic structures such as coronal mass ejections (CMEs) and CME–driven shocks (Wijsen et al. 2023a), also play vital roles in space weather research. To further refine and enhance our model, more realistic background structures and processes (e.g., CMEs) should be incorporated. More sophisticated and physically consistent descriptions of microscopic turbulence should also be considered since the mean free path was constant in our model. Additionally, simulations covering multiple species of SEPs should be conducted to comprehensively validate and improve the model.

Our next step in research is to verify and enhance the model simulation and prediction capabilities by incorporating more observational events that include the HCS and CIRs. Furthermore, we noted that there might be strong magnetic turbulence near the HCS. Our current model adopts a simplistic form of the diffusion coefficient and does not account for the turbulence near the HCS. We will conduct further research on this issue to strengthen our understanding of the HCS on SEP transport.

Acknowledgements. The present work is jointly supported by NSFC grants No. U2106201, No.42330210, Taishan Scholar Project of Shandong Province No. 202103143 and the National Key *R&D* Program of China (grant Nos. 2022YFF0503800 and 2021YFA0718600).

References

Altschuler, M. D. & Newkirk, G. 1969, Solar Phys., 9, 131

Arge, C. N., Odstrcil, D., Pizzo, V. J., & Mayer, L. R. 2003, in American Institute of Physics Conference Series, Vol. 679, Solar Wind Ten, ed. M. Velli, R. Bruno, F. Malara, & B. Bucci, 190–193

Battarbee, M., Dalla, S., & Marsh, M. S. 2017, ApJ, 836, 138

Battarbee, M., Dalla, S., & Marsh, M. S. 2018, ApJ, 854, 23

Bobik, P., Boschini, M. J., Della Torre, S., et al. 2016, J. Geophys. Res. Space Physics, 121, 3920

Burger, R. A. 2012, ApJ, 760, 60

Burger, R. A., Moraal, H., & Webb, G. M. 1985, Astrophys. Space Sci., 116, 107

Burger, R. A. & Potgieter, M. S. 1989, ApJ, 339, 501

Cohen, C. M. S., Christian, E. R., Cummings, A. C., et al. 2020, ApJS, 246, 20

Dalla, S., De Nolfo, G. A., Bruno, A., et al. 2020, A&A, 639, A105

Dalla, S., Marsh, M., Kelly, J., & Laitinen, T. 2013, J. Geophys. Res. Space Physics, 118, 5979

Desai, M. I., Drake, J. F., Phan, T., et al. 2025, ApJL, 985, L38

Desai, M. I., Mitchell, D. G., McComas, D. J., et al. 2022, ApJ, 927, 62

Eselevich, V. & Filippov, M. 1988, Planet. Space Sci., 36, 105

Feng, X. S., Wu, S. T., Wei, F. S., & Fan, Q. L. 2003, Space Sci. Rev., 107, 43

Feynman, J. & Gabriel, S. B. 2000, J. Geophys. Res. Space Physics, 105, 10543

Grechnev, V. V., Kurt, V. G., Chertok, I. M., et al. 2008, Solar Phys., 252, 149

Hoeksema, J. T. 1995, Space Sci. Rev., 72, 137

Hoeksema, J. T., Wilcox, J. M., & Scherrer, P. H. 1983, J. Geophys. Res. Space Physics, 88, 9910

Houeibib, A., Pantellini, F., & Griton, L. 2025, A&A, 694, A211

Isenberg, P. A. 1997, J. Geophys. Res. Space Physics, 102, 4719

Kallenrode, M.-B. 1993, J. Geophys. Res., 98, 5573

Kopp, A., Büsching, I., Strauss, R. D., & Potgieter, M. S. 2012, Comput. Phys. Commun., 183, 530

Lario, D., Wijsen, N., Kwon, R. Y., et al. 2022, ApJ, 934, 55

Le Roux, J. A. & Webb, G. M. 2009, ApJ, 693, 534

Li, G., Miao, B., Hu, Q., & Qin, G. 2011, Phys. Rev. Lett., 106, 125001

Liou, K. & Wu, C.-C. 2021, ApJ, 920, 39

Liou, K. & Wu, C.-C. 2024, ApJ, 966, 16

Ness, N. F. & Wilcox, J. M. 1965, Science, 148, 1592

Park, J., Bucik, R., Jeong, H.-J., & Moon, Y.-J. 2024, ApJ, 977, 86

Parker, E. N. 1958, ApJ, 128, 664

Pei, C., Bieber, J. W., Burger, R. A., & Clem, J. 2012, ApJ, 744, 170

Phan, T. D., Romeo, O. M., Drake, J. F., et al. 2025, ApJ, 986, 209

Potapov, A. S. 2018, Astrophys. Space Sci., 363, 81

Potgieter, M. 2013, Living Rev. Sol. Phys., 10

Qin, G. & Shen, Z.-N. 2017, ApJ, 846, 56

Qin, G., Zhang, M., Dwyer, J. R., Rassoul, H. K., & Mason, G. M. 2005, ApJ, 627, 562
Reames, D. V. 2017, Lecture Notes in Physics, Vol. 932, Solar Energetic Particles: A Modern Primer on Understanding Sources, Acceleration and Propagation (Cham: Springer)
Reid, G. C. 1964, J. Geophys. Res., 69, 2659
Richardson, I. G. 2004, Space Sci. Rev., 111, 267
Roelof, E. C. & Krimigis, S. M. 1973, J. Geophys. Res., 78, 5375
Schatten, K. H., Wilcox, J. M., & Ness, N. F. 1969, Solar Phys., 6, 442
Shen, F., Feng, X., & Song, W. 2009, Sci. China E: Technol. Sci., 52, 2895
Shen, F., Feng, X., Wu, S. T., & Xiang, C. 2007, J. Geophys. Res. Space Physics, 112, 2006JA012164
Shen, F., Yang, Z., Zhang, J., Wei, W., & Feng, X. 2018, ApJ, 866, 18
Shi, C., Velli, M., Tenerani, A., Réville, V., & Rappazzo, F. 2022, ApJ, 928, 93
Silwal, A., Zhao, L., Zank, G. P., et al. 2024, ApJ, 972, 168
Skilling, J. 1971, ApJ, 170, 265
Smith, E. J. 2001, J. Geophys. Res. Space Physics, 106, 15819
Smith, E. J. & Wolfe, J. H. 1979, Space Sci. Rev., 23, 217
Starkey, M. J., Dayeh, M. A., Desai, M. I., et al. 2024, ApJ, 962, 160
Steinolfson, R. S. & Mullan, D. J. 1980, ApJ, 241, 1186
Strauss, R. D., Potgieter, M. S., Büsching, I., & Kopp, A. 2012, Astrophys. Space Sci., 339, 223
Strauss, R. D. T. & Effenberger, F. 2017, Space Sci. Rev., 212, 151
Szabo, A., Larson, D., Whittlesey, P., et al. 2020, ApJS, 246, 47
Thomas, B. T. & Smith, E. J. 1981, J. Geophys. Res. Space Physics, 86, 11105
Tsurutani, B. T., Lakhina, G. S., Winterhalter, D., et al. 1999, Nonlinear Process. Geophys., 6, 235
Uralova, S. V. & Uralov, A. M. 1994, Solar Phys., 152, 457
Wang, L. D., Wang, Y., Wei, F. S., et al. 2025, ApJ, 985, 113
Waterfall, C. O. G., Dalla, S., Laitinen, T., Hutchinson, A., & Marsh, M. 2022, ApJ, 934, 82
Waterfall, C. O. G., De Nolfo, G. A., Hutchinson, A., et al. 2025, ApJ, 991, 104
Wei, W., Zhuang, B., Huang, J., et al. 2022, J. Geophys. Res. Space Physics, 127, e2022JA030652
Wijsen, N., Aran, A., Sanahuja, B., Pomoell, J., & Poedts, S. 2020, A&A, 634, A82
Wijsen, N., Lario, D., Sánchez-Cano, B., et al. 2023a, ApJ, 950, 172
Wijsen, N., Li, G., Ding, Z., et al. 2023b, JGR Space Physics, 128, e2022JA031203
Wu, C., Liou, K., Vourlidas, A., et al. 2016, J. Geophys. Res. Space Physics, 121, 56
Xu, X. & Xu, J. 2024, Phys. Fluids, 36, 087113
Yermolaev, Y. I., Nikolaeva, N. S., Lodkina, I. G., et al. 2010, Saint-Malo, (France), 648–651
Zhang, M., Qin, G., & Rassoul, H. 2009, ApJ, 692, 109
Zhang, Z., Artemyev, A. V., & Angelopoulos, V. 2025, Phys. Rev. E, 112, 015209